nature geoscience

ARTICLES

PUBLISHED ONLINE: 19 DECEMBER 2016 | DOI: 10.1038/NGEO2857

Subduction megathrust creep governed by pressure solution and frictional–viscous flow

Åke Fagereng[1,2]* and Sabine A. M. den Hartog[3]†

Subduction megathrust slip speeds range from slow creep at plate convergence rates (centimetres per year) to seismic slip rates (metres per second) in the largest earthquakes on Earth. The deformation mechanisms controlling whether fast slip or slow creep occurs, however, remain unclear. Here, we present evidence that pressure solution creep (fluid-assisted stress driven mass transfer) is an important deformation mechanism in megathrust faults. We quantify megathrust strength using a laboratory-constrained microphysical model for fault friction, involving viscous pressure solution and frictional sliding. We find that at plate-boundary deformation rates, aseismic, frictional–viscous flow is the preferred deformation mechanism at temperatures above 100 °C. The model thus predicts aseismic creep at temperatures much cooler than the onset of crystal plasticity, unless a boundary condition changes. Within this model framework, earthquakes may nucleate when a local increase in strain rate triggers velocity-weakening slip, and we speculate that slip area and event magnitude increase with increasing spacing of strong, topographically derived irregularities in the subduction interface.

Understanding why some megathrust segments accommodate displacement by earthquake slip versus aseismic creep is a major challenge. Geophysically observed variation in seismic style along active subduction megathrusts, involving a continuum of slip speeds from plate-boundary creep rates to earthquake slip[1], arises from processes within a fault zone in subducting sediments on top of potentially rugged ocean floor[2–6]. Dominantly creeping margins are characterized by low seismic coupling coefficients—the observed seismic moment release rate over that required by plate motion vectors—and lack of earthquake moment magnitudes $\geq$8.0 (Supplementary Fig. 1)[7,8]. Thus, some margins produce small-to-medium magnitude earthquakes, but the total moment of these earthquakes is insufficient to explain total geodetically observed displacement, and they must therefore be accompanied by aseismic creep[9].

The megathrust interface is commonly inferred as seismogenic to a depth where temperature exceeds the 350 °C required for crystal plasticity in quartz, or to the intersection with the hanging wall Moho, whichever is shallower[10]. However, geodetic inversions[8,11–14] reveal aseismic creep shallower than both the 350 °C isotherm and the hanging wall Moho. The question thus arises: how do some megathrust segments, such as north Hikurangi[11], the southern Japan Trench[12], southern New Hebrides[13], southern Kermadec Arc[13], and the Manila Trench[14] accommodate detectable displacement by aseismic creep in addition to moderate-size earthquakes, both originating at a similar depth range? This observation requires average creep rates of centimetres per year at temperatures less than 350 °C. Identifying the associated creep mechanism is critical for recognizing where megathrust displacement can occur without great earthquakes and, conversely, interpreting where great earthquakes may occur.

The mechanism of creep at seismogenic zone conditions

Tectonic mélanges comprising sheared trench-fill and ocean floor sediments have been interpreted as megathrust fault rocks (Fig. 1a)[3–6,15]. Deformation structures developed at seismogenic pressure–temperature (P–T) conditions include both discontinuities, such as faults and tensile fractures, and continuous structures, such as folds, boudins and foliations. One possible interpretation is that faults and associated fractures represent seismic deformation styles, whereas continuous features characterize slower, distributed, aseismic mechanisms recorded as creep[5,6,15]. In this interpretation, the mechanism accommodating deformation in continuous structures is responsible for aseismic creep.

In exhumed subduction thrusts, cleavage defined by fine-grained phyllosilicates wraps around rigid quartz clasts (Fig. 1b). Comparable microstructures are reported in borehole samples from the creeping segment of the continental San Andreas transform fault[16,17]. Mass balance calculations on San Andreas samples indicate pressure solution, involving fluid-assisted, stress-driven mass transfer, as the cleavage-forming process[16]. If empirical rates can be extrapolated, pressure solution is fast enough to account for aseismic sliding[16,18].

Pressure solution is also widely inferred as the dominant cleavage-forming process in mudrocks and phyllites sampled from exhumed subduction thrusts[6,19–21]. As an example, we consider a sample representative of sheared, cleaved mudstone from an inferred exhumed megathrust in the Chrystalls Beach Complex, New Zealand[21] (Fig. 1a–e), where cleavage defined by illite–muscovite developed at $T < 300$ °C (ref. 22). In this sample, cleavage seams are depleted in Si and enriched in Al (Fig. 1c and Supplementary Fig. 2). If cleavage develops by pressure solution, more soluble elements, such as Si, are dissolved, whereas less soluble elements, such as Al, are retained. Thus, the observations in the Chrystalls Beach sample are consistent with cleavage formation by pressure solution. Stress shadows around quartz clasts lack evidence for opening of pore space (Fig. 1d), and are sites of local silica enrichment (Fig. 1e). In addition to the formation of phyllosilicate cleavage, mass-transfer processes are therefore illustrated by silica enrichment and clast elongation through mineral growth in pressure shadows (Fig. 1d,e).

[1]School of Earth & Ocean Sciences, Cardiff University, Cardiff CF10 3AT, UK. [2]Department of Geological Sciences, University of Cape Town, Private Bag X3, Rondebosch 7701, South Africa. [3]HPT Laboratory, Department of Earth Sciences, Utrecht University, Utrecht, The Netherlands. †Present address: Rock Deformation Laboratory, School of Environmental Sciences, University of Liverpool, Liverpool, UK. *e-mail: FagerengA@cardiff.ac.uk

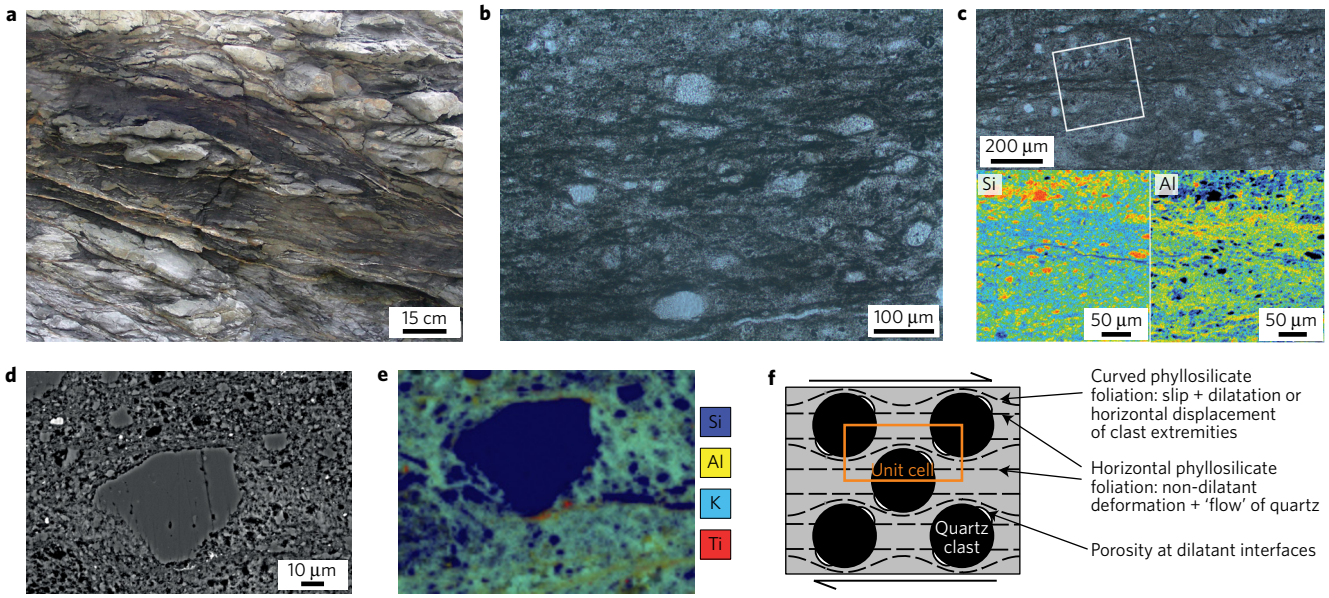

Figure 1 | Example of pressure-solution microstructures in a sample from the Chrystalls Beach Complex, New Zealand. a, Photograph of outcrop-scale mélange shear zone with sandstone lenses in cleaved mudstone matrix. **b**, Photomicrograph (plane-polarized light) of sample from mélange matrix, cleavage wraps around quartz clasts. **c**, A close-up of cleavage seams, the white rectangle shows the location of the element maps of Si and Al below; warm and cold colours show high and low relative abundance, respectively. **d**,**e**, Backscatter electron image of quartz clasts in phyllosilicate matrix (**d**), accompanied by a composite element map (**e**). **f**, Model microstructure where the matrix (grey) deforms by frictional sliding along foliations (dashed lines), and clasts (black) deform by pressure solution[25]. All panels show dextral sense of shear.

Microphysical model for fault gouge strength

The observations on exhumed megathrust rocks indicate that one of the microscopic processes that controls macroscopic frictional behaviour is viscous pressure solution. Indeed, microphysical modelling studies have shown that experimental observations on shear deformation at low strain rates in rocks comprising rigid clasts in a phyllosilicate matrix can be explained by frictional–viscous flow: frictional sliding along cleavage planes coupled to viscous (time-dependent) pressure solution of intervening rigid clasts[23–25]. The microstructures reported in these experimental studies are essentially identical to those seen in samples from the exhumed Chrystalls Beach Complex (Fig. 1b–e). Frictional–viscous flow is restricted to low strain rates (and/or high T); at higher strain rates (or lower T), slip is activated on anastomosing phyllosilicates, and microphysical models predict the importance of compaction by pressure solution[24,25]. Here, we use the model by Den Hartog and Spiers[25], coupled to analytical thermal gradients[26] (Methods), to predict megathrust shear strength. This microphysical model is based on friction experiments performed on materials and at conditions representative of subduction megathrusts. Following this model, we assume a matrix-supported megathrust shear zone where frictional sliding occurs on aligned phyllosilicates, accommodated by pressure solution shear of intervening quartz grains or dilatation (Fig. 1f). In this model, the relation between shear strain rate and shear stress is derived by considering stress balances at the microscale for a unit cell defined in Fig. 1f. The megathrust shear strain rate ($\dot{\gamma}$) is related to the slip velocity (V) assuming strain is distributed through a shear zone thickness (w)—therefore, $\dot{\gamma} = V/w$.

Each unit cell consists of quartz clasts, which are uniformly distributed such that horizontal rows overlap, and phyllosilicate foliations, which are on average parallel to the shear plane, but locally curve around rigid clasts (ref. 25; Fig. 1f and Supplementary Fig. 3), resembling the natural microstructure (Fig. 1b). Slip along foliation is assumed to be a frictional process governed by the frictional resistance of phyllosilicates, which varies with temperature and normal stress according to experimental data for illite and muscovite[27–31] (Methods). Depending on the conditions (for example, slip velocity, temperature, normal stress), the frictional resistance predicted by the model either decreases (velocity weakening) or increases (velocity strengthening) as slip accelerates. Whereas velocity-weakening behaviour is potentially unstable, and can promote fast earthquake slip, velocity-strengthening behaviour is inferred to lead to stable sliding, recorded as aseismic creep[32–34]. In the microphysical model used here[25], velocity-strengthening flow occurs when easy shear of quartz clasts by thermally activated pressure solution, in series with rate-independent slip on planar phyllosilicates, leads to non-dilatant deformation (frictional–viscous flow). Velocity-weakening slip occurs when difficult pressure solution shear of quartz results in increased shear stress and slip is activated on curved phyllosilicate cleavages. This slip along curved foliation results in dilatation at the clast–matrix interface under extension (Fig. 1f), which at steady state is balanced by compaction via pressure solution.

Application of flow law to natural subduction zones

We apply boundary conditions appropriate for the northern Hikurangi margin, a megathrust shown to deform predominantly by aseismic creep, at least over the past few decades[11]. Pore fluid factors ($\lambda = P_f/\sigma_v$, where P_f is pore fluid pressure and σ_v is vertical stress) of 0.8 and 0.95 are imposed to test variations between moderate and high fluid pressure conditions. We distribute a steady creep rate of 40 mm yr^{-1} over a subduction thrust shear zone of thickness 1–100 m, a range representing strain rates from 10^{-11} to 10^{-9} s^{-1}, and a range in deforming thickness typical of exhumed mélanges and drilled subduction megathrusts[15]. Quartz grain size varies from 10 to 100 µm, based on an examination of Fig. 1b–e. All model parameters are listed in Supplementary Table 1.

The frictional–viscous flow strength of quartz–phyllosilicate mixtures as a function of depth is compared to frictional strengths of mono-mineralic quartz and illite–muscovite faults (Fig. 2a,b). At all considered conditions, frictional sliding in quartz requires higher shear stress than any slip mechanism in phyllosilicates or quartz–phyllosilicate mixtures; we therefore note that frictional sliding in quartz is an unlikely deformation mechanism in phyllosilicate-rich

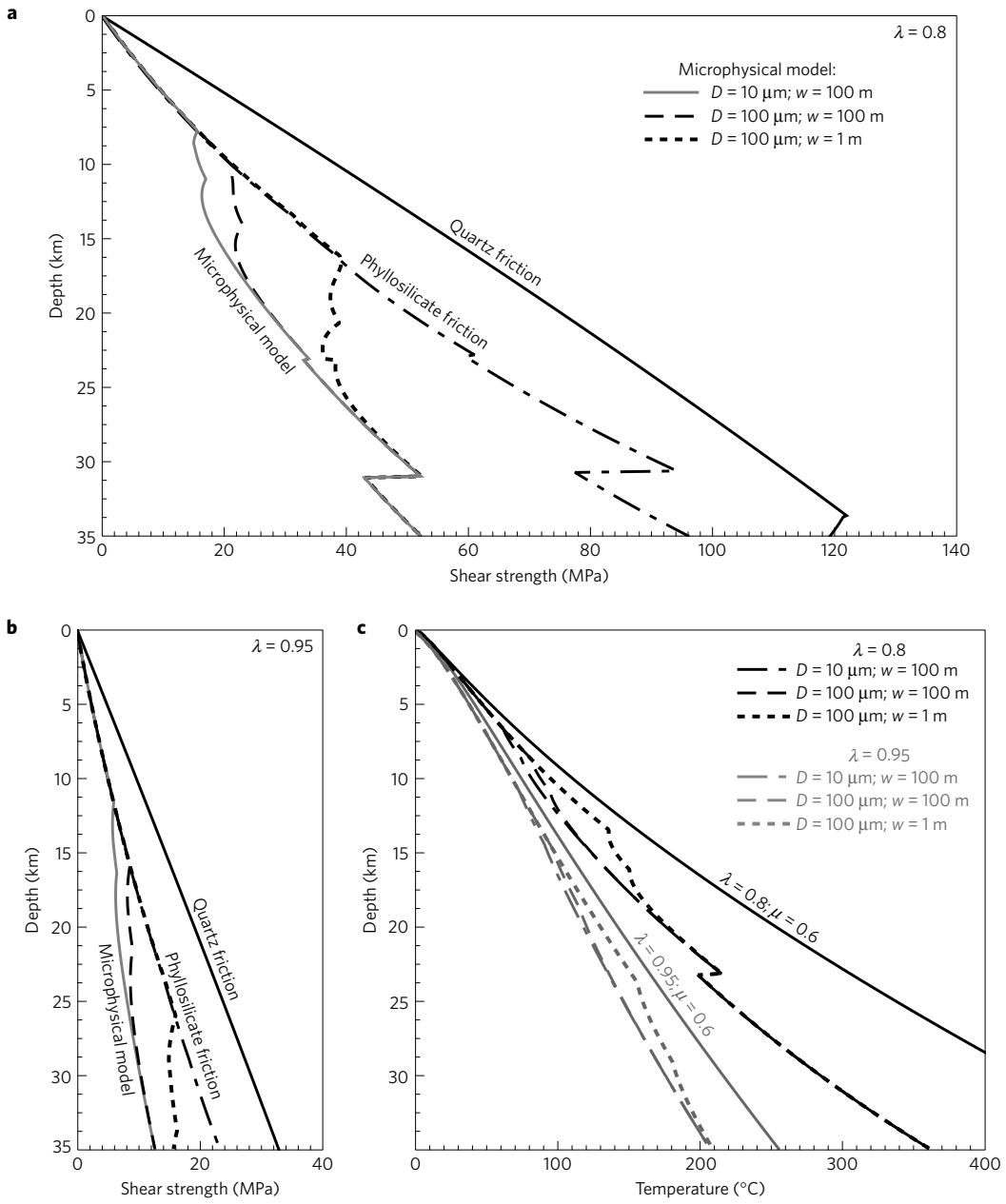

Figure 2 | Strength curves calculated along a subduction thrust interface with properties representative of the northern Hikurangi margin. a,**b**, Strength curves versus depth. The pore fluid factor $\lambda = P_f/\sigma_v$, where P_f is pore fluid pressure and σ_v is vertical stress, is moderate (0.8) in **a** and high (0.95) in **b**. The curves labelled 'microphysical model' represent the strength of a fault where deformation occurs by slip on phyllosilicate surfaces and pressure solution of intervening quartz. **c**, Profiles of depth versus temperature, including the initial thermal structure where the frictional coefficient, μ, is 0.6. In all plots the microphysical model predictions depend on grain size, D, and shear zone thickness, w, as shown in the legend. Supplementary Table 1 reports the full list of parameters.

megathrust shear zones. For both high and moderate fluid overpressure, there is a depth below which frictional–viscous flow requires a lower shear stress than that required for frictional sliding in mono-mineralic phyllosilicate fault gouges (Fig. 2a,b). For deforming zones of 100 m thickness, frictional–viscous flow becomes favourable at 8–10 km depth in moderate fluid pressure conditions (Fig. 2a), and at 12–16 km depth under high fluid pressure (Fig. 2b). In both cases, frictional–viscous flow becomes favourable at $T \geq 100 \pm 20\,^{\circ}C$ (Fig. 2c), where the corresponding shear stress, τ, is $\leq$10 MPa at high fluid pressure, and $\leq$20 MPa at moderate fluid pressure (Fig. 2a,b). For a 1-m-thick deforming zone, higher strain rates make frictional–viscous flow less favourable; at high fluid pressure, frictional sliding of phyllosilicates remains favourable until a depth of ~26 km ($T < 200\,^{\circ}C$, $\tau < 20$ MPa), whereas at lower fluid pressures, frictional sliding also requires higher stresses and frictional–viscous flow becomes favourable from 16 km depth ($T < 150\,^{\circ}C$, $\tau \sim 40$ MPa).

Calculated temperatures define low thermal gradients, partly because very low stresses reduce temperatures relative to models with Byerlee friction (Fig. 2c). In our warmest model, where $\lambda = 0.8$, the shear zone width is 1 m and the quartz grain size is 100 μm, shear heating makes up approximately 30% of the heat budget; for the coldest model, where $\lambda = 0.95$, the shear zone width is 100 m and the quartz grain size is 10 μm, less than 10% of the heat budget is contributed by shear heating. Hikurangi is also a cool margin in the global spectrum of subduction zone thermal models, where model

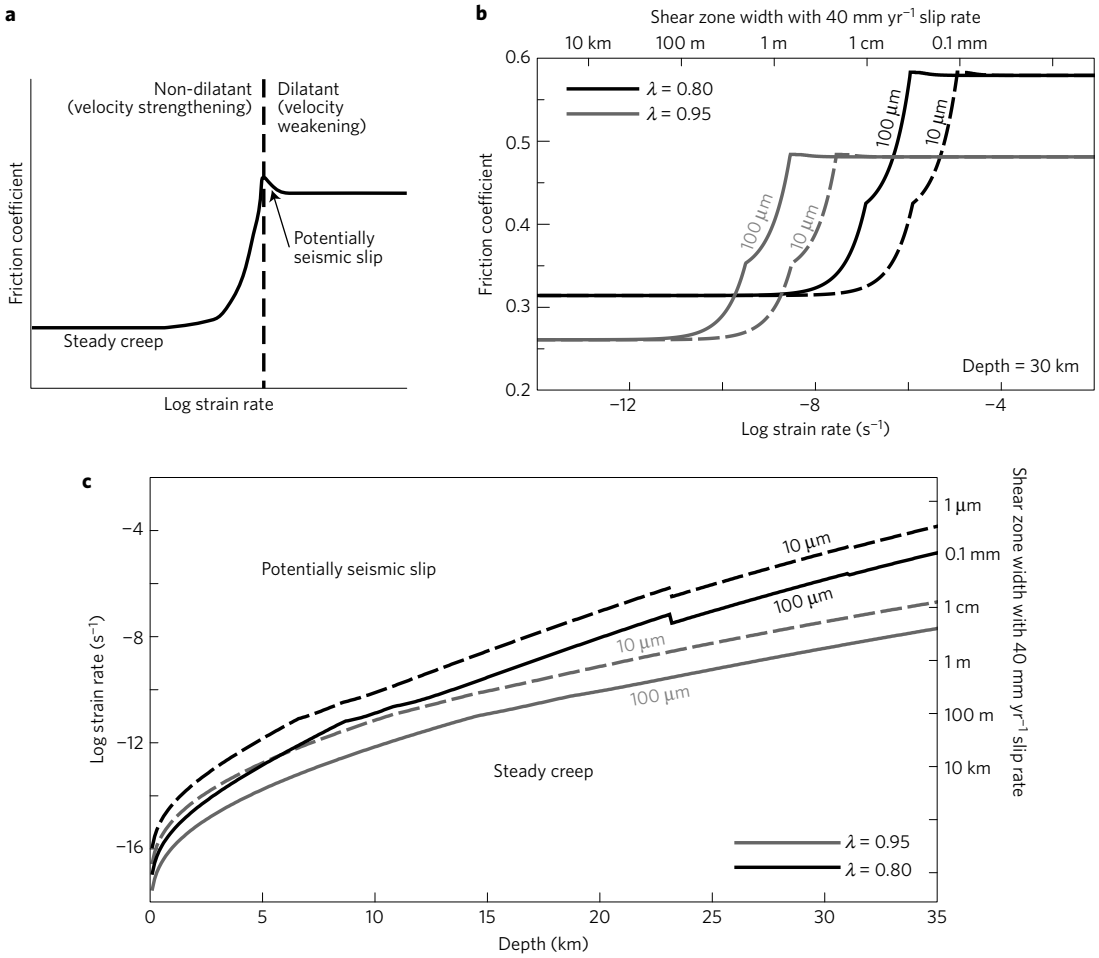

Figure 3 | Relations between slip velocity and frictional behaviour. a, Schematic relationship between friction coefficient and strain rate in the microphysical model used here, indicating a change from velocity strengthening to velocity weakening at high strain rate[25]. **b**, Friction coefficient at a fixed depth of 30 km, as a function of strain rate or shear zone width at a fixed slip velocity. **c**, Plot that quantifies the strain rate and shear zone width, where a change from velocity strengthening to velocity weakening is predicted, as a function of depth (parameters as in Fig. 2).

temperatures[35] compare to Fig. 2c. Compared to a recent numerical model[36], calculations here with $\lambda = 0.8$ are cooler at depths below ~10 km, whereas $\lambda = 0.95$ gives consistently lower temperatures.

Aseismic frictional–viscous flow is the predicted deformation style at $T \geq 100\,^{\circ}C$, when average plate-boundary shear strain rates are accommodated in a shear zone hundreds of metres in thickness (Fig. 2a,b). Generation of runaway earthquake slip requires a change in these boundary conditions. This is because, at low strain rates, pressure solution of quartz clasts accommodates local finite strain around the rigid clasts created by slip on surrounding, planar phyllosilicate cleavages (Figs 1d,e and 3a,b)[25]. At higher strain rate, pressure solution requires greater driving stress, bulk fault zone strength increases, and eventually dilatant, velocity-weakening behaviour occurs, allowing potentially unstable slip[25] (Fig. 3a,b). At each depth increment in Fig. 2, we calculate the friction coefficient as a function of strain rate, as shown for a depth of 30 km in Fig. 3b. The strain rate required for a change from velocity-strengthening to velocity-weakening behaviour increases with depth (Fig. 3c). At depths greater than 15 km, where frictional–viscous flow generally becomes favourable (Fig. 2), velocity-strengthening behaviour occurs at strain rates slower than $10^{-12}\,s^{-1}$ and shear zone widths greater than tens of metres at 40 mm yr^{-1} slip rates (Fig. 3c). At a depth of 30 km, where frictional–viscous flow is preferred for all our considered conditions with a plate-boundary slip rate (Fig. 2a,b), the shear strain rates required for velocity-weakening behaviour range from 10^{-9} to $10^{-4}\,s^{-1}$ (Fig. 3b,c).

At shallow depths, although commonly interpreted as a velocity-strengthening region[10,34], potentially seismic slip is predicted at strain rates as low as $10^{-12}\,s^{-1}$ at 5 km depth, and $10^{-16}\,s^{-1}$ at the surface (Fig. 3c). This is because shear deformation by pressure solution of quartz is difficult at low temperature, yielding dilatant behaviour. At greater depths, where $T \geq 100 \pm 20\,^{\circ}C$, low-strain-rate frictional–viscous flow is the predicted deformation mechanism (Fig. 2), because a high quartz solubility yields efficient dissolution and re-precipitation at this temperature (ref. 37, Supplementary Fig. 4). This potential change in deformation mechanism is reflected in exhumed accretionary prisms, where mélange deformation at $T < 100\,^{\circ}C$ is dominated by distributed cataclasis, whereas a pressure solution cleavage and localized slip surfaces are prevalent in rocks deformed at $T > 150\,^{\circ}C$ (refs 6,21,38,39). In central and northern Hikurangi, the margin we used for our thermal calculations, it is uncertain whether a near-surface velocity-strengthening zone and updip limit of seismicity is present, as slow slip events may propagate to the trench[40]; the downdip limit of the interseismically locked zone is here at less than 10 km depth[11]. This downdip limit of the locked zone is in agreement with the onset of velocity-strengthening frictional–viscous flow at 10 km depth and $T \leq 100\,^{\circ}C$, in a margin of moderate fluid overpressure and distributed shear (Fig. 2a,c).

Following ref. 25, we conclude that frictional–viscous flow involving pressure solution is a viable mechanism of velocity-strengthening, stable creep. We consider the recently discovered

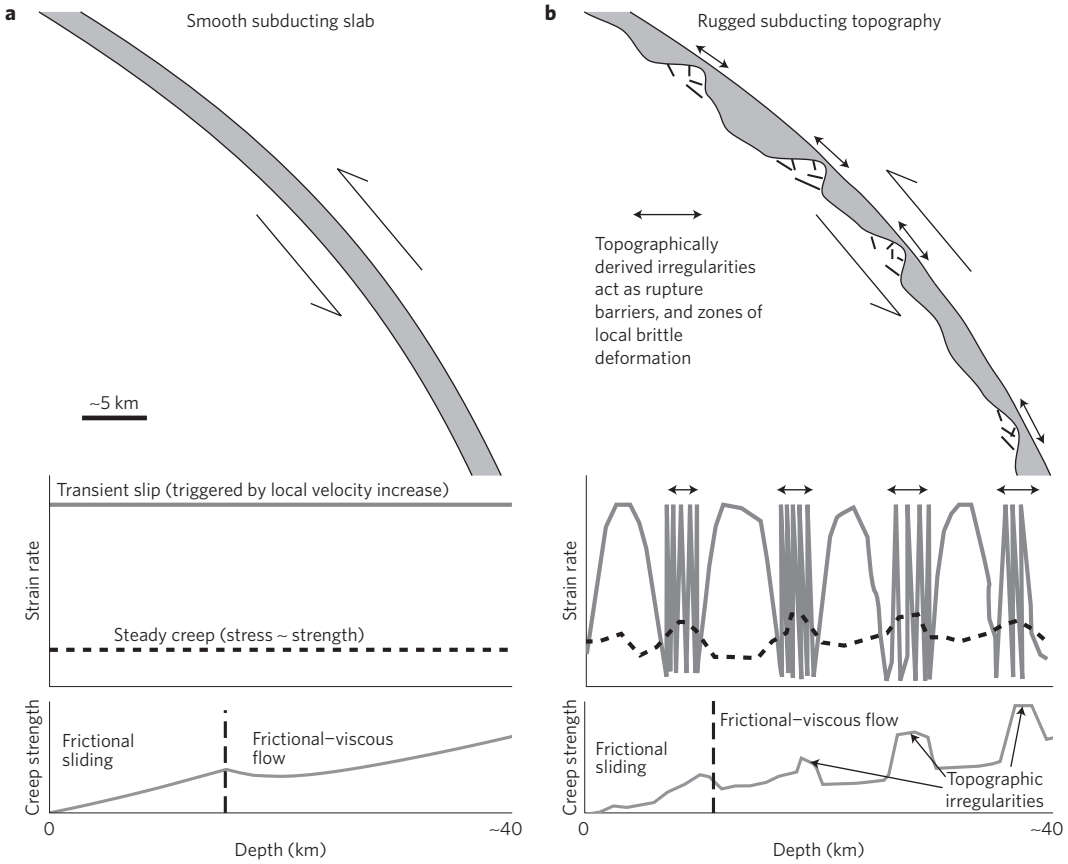

Figure 4 | Representations of the effect of frictional–viscous flow on megathrust seismic style. Subduction interfaces related to smooth (**a**) and rugged (**b**) topography on subducting oceanic crust. Inferred transient and steady-state strain rate variations along these interfaces are shown below, as is the inferred depth versus creep strength profile as based on Fig. 2 and downdip variation in shear zone width.

phenomenon of slow slip along subduction megathrusts[41,42], defined as geodetically observed displacement that is faster than plate convergence rates but too slow to generate seismic waves, as a form of unstable slip[43]. Shallow slow slip, as observed near the trench in northern Hikurangi[40], may therefore be a manifestation of unstable, dilatant shear at $T < 100\,^{\circ}\mathrm{C}$ (the 'potentially seismic slip' in Fig. 3c). Deeper slow slip events occurring downdip of the locked zone and at depths $\geq$30 km, such as in Cascadia, are either independent of, or possibly load, the seismogenic region[44]. The application of the microphysical model predicts velocity-strengthening behaviour at such depths; thus, as for earthquakes, slow slip faster than steady-state plate convergence rates requires a local change in conditions, possibilities of which we discuss in the next section. Under the local triggering conditions, slow slip probably reflects competition between deformation modes within a heterogeneous fault zone[45], but may be an expression of either localized frictional sliding or distributed shearing flow; differentiating between these basic geometries requires currently missing knowledge of the deforming thickness during slow slip events.

Relating creep to subducting slab topography

Large earthquakes ($M_w \geq 8.0$) have been associated with subduction of smooth sea floor, because a lack of barriers to slip—such as local topography, seamounts, and horst-and-graben structures—allows for large rupture areas[2,46]. By comparison, subduction of rugged ocean floor has been suggested to lead to smaller earthquakes because rupture areas are geometrically constrained[2,12,36]. We therefore consider the implications of the model results for two endmember subducting plates, with either smooth or rugged topography[2,36,46].

For the first case, smooth subducting slabs lack geometrical barriers to rupture propagation and the fault zone has similar thickness and strain rate at all depths (Fig. 4a). However, small-scale heterogeneities may locally elevate strain rates, causing velocity-weakening behaviour (Fig. 3b,c), and triggering rupture propagation over a large area without hindrance by large-scale barriers[4]. For the second case, rugged subducting ocean floor also deforms predominantly via creep by frictional–viscous flow, and small-scale heterogeneities may again lead to local velocity-weakening behaviour. However, in this case, strong, topographically derived irregularities on the interface create barriers to earthquake propagation, constraining earthquakes to smaller slip areas, and therefore moderate magnitudes (Fig. 4b). At and around such barriers, local brittle deformation occurs to accommodate subduction of the topographic feature[2,12]. Extrapolating from continental strike slip faults[47], we suggest that geometrical barriers—such as deformed, subducting seamounts—that result in a discontinuity of potential slip surfaces by more than ~4 km, are likely to arrest rupture propagation. Moreover, because of numerous stress and strain-rate peaks, megathrusts associated with rugged subducting topography may appear strong in stress calculations from heat flow measurements[36] or Coulomb wedge mechanics[48], relative to fault segments where smooth subducting slabs allow large slip areas on a through-going weak surface or a system of anastomosing slip surfaces. A caveat to this broad, endmember interpretation is that subducting topography and megathrust structure may evolve with depth. For example, subducting seamounts may be progressively destroyed if they are indeed areas of increased brittle deformation[2], and the microscale geometry within the fault zone can change via the development of through-going fault surfaces, mineral precipitation and reactions,

and evolving grain shapes and sizes, via progressive deformation, metamorphism and fluid flow[49]. As such, the subduction thrust is a dynamic structure, displacing a footwall with inherently complex geometry, and accurate predictions require high-resolution subsurface data.

In summary, our model offers an explanation for why megathrusts creep in some places, and slip seismically in others. It implies that creep by frictional–viscous flow is the preferred deformation mechanism of most if not all subduction thrust interfaces, below some depth determined by thermal structure, strain rate and fluid pressure (Figs 2 and 3 and Supplementary Fig. 4). However, earthquakes may nucleate at local heterogeneities where the behaviour is velocity-weakening[50]. Slip area and earthquake magnitude should then depend on the spacing of strong, topographically derived irregularities in the subduction interface, with giant earthquakes requiring this spacing to be large.

Methods

Methods, including statements of data availability and any associated accession codes and references, are available in the online version of this paper.

Received 11 March 2016; accepted 14 November 2016; published online 19 December 2016

References

1. Peng, Z. & Gomberg, J. An integrated perspective of the continuum between earthquakes and slow slip phenomena. *Nat. Geosci.* **3,** 599–607 (2010).
2. Wang, K. & Bilek, S. L. Do subducting seamounts generate or stop large earthquakes? *Geology* **39,** 819–822 (2011).
3. Shreve, R. L. & Cloos, M. Dynamics of sediment subduction, mélange formation, and prism accretion. *J. Geophys. Res.* **91,** 10229–10245 (1986).
4. Bachmann, R. *et al*. Exposed plate interface in the European Alps reveals fabric styles and gradients related to an ancient seismogenic coupling zone. *J. Geophys. Res.* **114,** B05402 (2009).
5. Fagereng, Å. & Sibson, R. H. Mélange rheology and seismic style. *Geology* **38,** 751–754 (2010).
6. Rowe, C. D., Meneghini, F. & Moore, J. C. in *Geology of the Earthquake Source: A Volume in Honour of Rick Sibson* (eds Fagereng, Å., Toy, V. G. & Rowland, J. V.) 77–95 (Geological Society of London, 2011).
7. Heuret, A., Lallemand, S., Funiciello, F., Pitomallo, C. & Faccenna, C. Physical characteristics of subduction interface type seismogenic zones revisited. *Geochem. Geophys. Geosyst.* **12,** Q01004 (2011).
8. Scholz, C. H. & Campos, J. The seismic coupling of subduction zones revisited. *J. Geophys. Res.* **117,** B05310 (2012).
9. Rubin, A. M., Gillard, D. & Got, J.-L. Streaks of microearthquakes along creeping faults. *Nature* **400,** 635–641 (1999).
10. Hyndman, R. D., Yamano, M. & Oleskevich, D. A. The seismogenic zone of subduction thrust faults. *Isl. Arc* **6,** 244–260 (1997).
11. Wallace, L. M. *et al*. Characterizing the seismogenic zone of a major plate boundary subduction thrust: Hikurangi Margin, New Zealand. *Geochem. Geophys. Geosyst.* **10,** Q10006 (2009).
12. Mochizuki, K., Yamada, T., Shinohara, M., Yamanaka, Y. & Kanazawa, T. Weak interplate coupling by seamounts and repeating M ∼ 7 earthquakes. *Science* **321,** 1194–1197 (2008).
13. Power, W., Wallace, L. M., Wang, X. & Reyners, M. Tsunami hazard posed to New Zealand by the Kermadec and Southern New Hebrides subduction margins: an assessment based on plate boundary kinematics, interseismic coupling, and historical seismicity. *Pure Appl. Geophys.* **169,** 1–36 (2012).
14. Hsu, Y.-J., Yu, S.-B., Song, T.-R. & Bacolcol, T. Plate coupling along the Manila subduction zone between Taiwan and northern Luzon. *J. Asian Earth Sci.* **51,** 98–108 (2012).
15. Rowe, C. D., Moore, J. C. & Remitti, F. IODP Exp. 343/343T Scientists. The thickness of subduction plate boundary faults from the seafloor into the seismogenic zone. *Geology* **41,** 991–994 (2013).
16. Gratier, J.-P. *et al*. Aseismic sliding of active faults by pressure solution creep: evidence from the San Andreas fault observatory at depth. *Geology* **39,** 1131–1134 (2011).
17. Richard, J., Gratier, J. P., Doan, M.-L., Boullier, A.-M. & Renard, F. Rock and mineral transformations in a fault zone leading to permanent creep: interactions between brittle and viscous mechanisms in the San Andreas Fault. *J. Geophys. Res.* **119,** 8132–8153 (2014).
18. Gratier, J.-P., Guiguet, R., Renard, F., Jenatton, L. & Bernard, D. A pressure solution creep law for quartz from indentation experiments. *J. Geophys. Res.* **114,** B03403 (2009).
19. Schwarz, S. & Stöckhert, B. Pressure solution in siliciclastic HP-LT rocks–constraints on the state of stress in deep levels of accretionary complexes. *Tectonophysics* **255,** 203–209 (1996).
20. Kawabata, K., Tanaka, H. & Kimura, G. Mass transfer and pressure solution in deformed shale of accretionary complex: examples from the Shimanto Belt, southwest Japan. *J. Struct. Geol.* **29,** 697–711 (2007).
21. Fagereng, Å. in *Geology of the Earthquake Source: A Volume in Honour of Rick Sibson* (eds Fagereng, Å., Toy, V. G. & Rowland, J. V.) 55–76 (Geological Society of London, 2011).
22. Fagereng, Å. & Cooper, A. F. The metamorphic history of rocks buried, accreted and exhumed in an accretionary prism: an example from the Otago Schist, New Zealand. *J. Metamorph. Geol.* **28,** 935–954 (2010).
23. Bos, B. & Spiers, C. J. Frictional-viscous flow of phyllosilicate-bearing fault-rock: microphysical model and implications for crustal strength profiles. *J. Geophys. Res.* **107,** 2028 (2002).
24. Niemeijer, A. & Spiers, C. J. in *High-Strain Zones: Structure and Physical Properties* (eds Bruhn, D. & Burlini, L.) 303–327 (Geological Society of London, 2005).
25. Den Hartog, S. A. M. & Spiers, C. J. A microphysical model for fault gouge friction applied to subduction megathrusts. *J. Geophys. Res.* **119,** 1510–1529 (2014).
26. Molnar, P. & England, P. Temperatures, heat flux and frictional stress near major thrust faults. *J. Geophys. Res.* **95,** 4833–4856 (1990).
27. Den Hartog, S. A. M., Saffer, D. M. & Spiers, C. J. The roles of quartz and water in controlling unstable slip in phyllosilicate-rich megathrust fault gouges. *Earth Planets Space* **66,** 78 (2014).
28. Den Hartog, S. A. M., Niemeijer, A. R. & Spiers, C. J. Friction on subduction megathrust faults: beyond the illite-muscovite transition. *Earth Planet. Sci. Lett.* **373,** 8–19 (2013).
29. Van Diggelen, E. W. E., De Bresser, J. H. P., Peach, C. J. & Spiers, C. J. High shear strain behaviour of synthetic muscovite fault gouges under hydrothermal conditions. *J. Struct. Geol.* **32,** 1685–1700 (2010).
30. Den Hartog, S. A. M. & Spiers, C. J. Influence of subduction zone conditions and gouge composition on frictional slip stability of megathrust faults. *Tectonophysics* **600,** 75–90 (2013).
31. Niemeijer, A. R., Spiers, C. J. & Peach, C. J. Frictional behaviour of simulated quartz fault gouges under hydrothermal conditions: results from ultra-high strain rotary shear experiments. *Tectonophysics* **460,** 288–303 (2008).
32. Dieterich, J. H. Modeling of rock friction: 1. Experimental results and constitutive equations. *J. Geophys. Res.* **84,** 2161–2168 (1979).
33. Marone, C. Laboratory-derived friction laws and their application to seismic faulting. *Annu. Rev. Earth Planet. Sci.* **26,** 643–696 (1998).
34. Scholz, C. H. Earthquakes and friction laws. *Nature* **391,** 37–42 (1998).
35. Syracuse, E. M., van Keken, P. E. & Abers, G. A. The global range of subduction zone thermal models. *Phys. Earth. Planet. Inter.* **183,** 73–90 (2010).
36. Gao, X. & Wang, K. Strength of stick-slip and creeping subduction megathrusts from heat flow observations. *Science* **345,** 1038–1041 (2014).
37. Tester, J. W., Worley, W. G., Robinson, B. A., Grigsby, C. & Feerer, J. L. Correlating quartz dissolution kinetics in pure water from 25 to 625 °C. *Geochim. Cosmochim. Acta* **58,** 2407–2420 (1994).
38. Hashimoto, Y., Nakaya, T., Ito, M. & Kimura, G. Tectonolithification of sandstone prior to the onset of seismogenic subduction zone: evidence from tectonic mélange of the Shimanto Belt, Japan. *Geochem. Geophys. Geosyst.* **7,** Q06013 (2006).
39. Moore, J. C., Rowe, C. D. & Meneghini, F. in *The Seismogenic Zone of Subduction Thrust Faults* (eds Dixon, T. H. & Moore, J. C.) 288–315 (Colombia Univ. Press, 2007).
40. Wallace, L. M. *et al*. Slow slip near the trench at the Hikurangi subduction zone, New Zealand. *Science* **353,** 701–704 (2016).
41. Dragert, H., Wang, K. & James, T. A silent slip event on the deeper Cascadia subduction interface. *Science* **292,** 1525–1528 (2001).
42. Obara, K., Hirose, H., Yamamizu, F. & Kasahara, K. Episodic slow slip events accompanied by non-volcanic tremors in southwest Japan subduction zone. *Geophys. Res. Lett.* **31,** L23602 (2004).
43. Liu, Y. & Rice, J. R. Aseismic slip transients emerge spontaneously in three-dimensional rate and state modelling of subduction earthquake sequences. *J. Geophys. Res.* **110,** B08307 (2005).
44. McCrory, P. A., Hyndman, R. D. & Blair, J. L. Relationship between the Cascadia fore-arc mantle wedge, nonvolcanic tremor, and the downdip limit of seismogenic rupture. *Geochem. Geophys. Geosyst.* **15,** 1071–1095 (2014).
45. Saffer, D. M. & Wallace, L. M. The frictional, hydrologic, metamorphic and thermal habitat of shallow slow earthquakes. *Nat. Geosci.* **8,** 594–600 (2015).
46. Ruff, L. Do trench sediments affect great earthquake occurrence in subduction zones? *Pure Appl. Geophys.* **129,** 263–282 (1989).

47. Wesnousky, S. G. Predicting the endpoints of earthquake ruptures. *Nature* **444,** 358–360 (2006).
48. Fagereng, Å. Wedge geometry, mechanical strength, and interseismic coupling of the Hikurangi subduction thrust, New Zealand. *Tectonophysics* **507,** 26–30 (2011).
49. Knipe, R. J. Deformation mechanisms—recognition from natural tectonites. *J. Struct. Geol.* **11,** 127–146 (1989).
50. Hicks, S. P. *et al*. The 2010 M_w 8.8 Maule, Chile earthquake: nucleation and rupture propagation controlled by a subducted topographic high. *Geophys. Res. Lett.* **39,** L19308 (2012).

Acknowledgements

Initial work on this project was funded through NRF Incentive Funding for Rated Researchers to Å.F. while at the University of Cape Town. We thank C. Tinguely (Cape Town) and D. Muir (Cardiff) for microprobe/SEM assistance, and A. Cross for a constructive review that significantly improved the manuscript.

Author contributions

Both authors contributed to designing the study, making the calculations, and writing the paper. Å.F. provided the microstructural observations.

Additional information

Supplementary information is available in the online version of the paper. Reprints and permissions information is available online at www.nature.com/reprints. Correspondence and requests for materials should be addressed to Å.F.

Competing financial interests

The authors declare no competing financial interests.

Methods

Element maps. Element maps (Fig. 1c–e and Supplementary Fig. 2) were plotted from energy dispersive spectroscopy (EDS) data, which give the relative abundance of elements, measured on a carbon-coated, 30-μm-thick sample. Maps in Fig. 1c were collected using an electron-probe microanalyser at the University of Cape Town, with beam conditions of 15 kV, 18.5 nA, 12 ms dwell time, and a spot size of 1 μm. Electron backscatter images in Fig. 1d and the map in Fig. 1e were acquired using a Zeiss Sigma HD scanning electron microscope in the School of Earth & Ocean Sciences at Cardiff University. The EDS data for these element maps were acquired with an beam accelerating voltage of 20 kV, nominal beam current of 4.7 nA, and a 20 ms dwell time. The resulting pixels are approximately 1 μm.

Pressure–temperature estimates. To calculate the shear stress predicted by the microphysical model as a function of depth, approximations of temperature, T, and effective normal stress, σ_n', as functions of depth are required. Because the subduction thrust interface is gently dipping, σ_n' is approximated as the effective vertical stress[51,52] so that:

$$\sigma_n' = \rho g z (1-\lambda) \tag{1}$$

where ρ is the average density of overlying rock, taken as 2,650 kg m^{-1}, a value typical of quartzofeldspathic rocks, g is gravitational acceleration, λ is the pore fluid factor defined in the main text, and z is depth.

Temperature (°C) is calculated according to the analytical derivation of Molnar and England[26], as previously applied to the Hikurangi margin[53], that sums advective, radiogenic and shear heating terms, where:

$$T = \frac{K_m}{SK_s}\frac{T_0 z}{\sqrt{\pi\kappa(t_0+t_s)}} + \frac{A_r z^2}{2SK_s} + \frac{\tau V z}{SK_s} \tag{2}$$

in which the dimensionless parameter S is defined as:

$$S = 1 + b\frac{K_m}{K_s}\sqrt{\frac{Vz\sin\delta}{\kappa}} \tag{3}$$

In these formulations, K_m and K_s are the mantle and accretionary prism conductivities, respectively, T_0 is the temperature at the base of the lithosphere, κ is the thermal diffusivity, t_0 is the age of the subducting oceanic crust at the trench, A_r is the average radioactive heat production rate in the forearc materials, τ is the shear stress, and b is a geometrical factor. t_s is the time to subduct the slab to depth z, approximated as $t_s = z/(V\sin\delta)$, where V is the slip velocity, assuming the megathrust accommodates the trench-normal component of the plate convergence vector, and δ is the average dip angle of the subduction thrust interface. Values for all the above parameters are listed in Supplementary Table 1. To obtain the shear heating term in the initial thermal structure, τ is estimated as σ_n' multiplied by a frictional coefficient of $\mu = 0.6$, estimating the lower end of the Byerlee range[54]. After calculating shear stress according to the microphysical model, the calculated shear stress as a function of depth is used to recalculate the thermal structure, which is then used to recalculate shear stress. The change in thermal structure from the first calculation to calculations involving shear stresses from the microphysical model can be seen in Fig. 2c.

Temperature-dependent mono-mineralic friction. Values for the friction coefficient for phyllosilicates were determined assuming the dominant phyllosilicate mineral to be illite and muscovite at temperatures below and above 300 °C, respectively, and by assuming that temperature rather than effective normal stress dominantly affects the friction coefficient. The friction coefficient of illite as a function of temperature was determined by fitting a linear trend line to a combination of data at 20 °C (ref. 55) and data at 200, 350 and 500 °C (ref. 27), all representing final friction values (at 9.21 and ~40 mm shear displacement, respectively) at a sliding velocity of 1 μm s^{-1}. Note that the sliding velocity at ~40 mm shear displacement in ref. 27 was 10 μm s^{-1}, and we thus recalculated it to 1 μm s^{-1} using the value for $\Delta\mu/\Delta\ln V$, or $(a\text{-}b)$, for a velocity step from 10 to 1 μm s^{-1} obtained in the same experiment. Similarly, the friction coefficient of muscovite as a function of temperature was determined by fitting two linear trend lines (joining at 600 °C) to data at 200, 400 and 600 °C (ref. 28) and data at 400, 500 and 700 °C (ref. 29). These data represent close to final friction coefficients, those from ref. 28 taken at a shear strain of 50 and recalculated for 1 μm s^{-1} by the method described for illite (ref. 28) and those from ref. 29 reported for the 0.5 μm s^{-1} step, which occurred at near steady-state friction. The resultant empirical function for phyllosilicate friction coefficient, μ_{ph}, becomes:

$$\mu_{ph}\begin{cases} 0.320 + 9.10\times10^{-4}T, & T < 300\,^\circ\mathrm{C} \\ 0.300 + 6.18\times10^{-4}T, & 300\,^\circ\mathrm{C} \le T < 600\,^\circ\mathrm{C} \\ 1.997 - 2.24\times10^{-3}T, & T \ge 600\,^\circ\mathrm{C} \end{cases} \tag{4}$$

This definition for the phyllosilicate friction coefficient was used to construct the strength profiles for pure phyllosilicates and as input to the microphysical model.

The friction coefficient of quartz, for plotting the frictional strength of mono-mineralic quartz aggregates in Fig. 2a,b, is estimated based on room temperature data[55], data at 140 °C (ref. 30) and data at 400–600 °C (ref. 31). Based on similar arguments as for creating an empirical function of phyllosilicate friction as a function of temperature, we obtain a function for quartz friction, μ_{qtz}:

$$\mu_{qtz}\begin{cases} 0.750 - 1.04\times10^{-4}T, & T < 500\,^\circ\mathrm{C} \\ 1.41 - 1.43\times10^{-3}T, & T \ge 500\,^\circ\mathrm{C} \end{cases} \tag{5}$$

Microphysical model[25]. The microphysical model used to calculate the strength profiles (Fig. 2) was derived by Den Hartog and Spiers[25]. The model describes the steady-state frictional behaviour of sheared illite–quartz mixtures, and assumes a matrix-supported shear zone consisting of phyllosilicates and quartz clasts (Supplementary Fig. 3). The quartz clasts are uniformly distributed, arranged such that horizontal rows of clasts overlap. On average, the phyllosilicates are aligned parallel to Y-shear bands, but locally anastomose around the rigid clasts. Note that the Y-shear bands considered in the model will on average be parallel to the megathrust interface, which implies that foliation that is parallel to these shear bands—described as 'horizontal' in the model—will be gently dipping in the megathrust setting.

Within the model microstructure, shear deformation occurs either within the 'clast body' zones containing a horizontal phyllosilicate foliation and quartz clasts (Type B zones, Supplementary Fig. 3) or in the 'clast overlap' regions containing anastomosing phyllosilicates and overlapping quartz clast edges (Type O zones, Supplementary Fig. 3). The horizontal foliation in the Type B zones abuts against the quartz clasts, so that sliding on this foliation requires serial simple shear of the clast 'bodies'. Shear of the clasts is assumed to occur by thermally activated deformation. By contrast, in the Type O zones, the foliation anastomoses around the clast 'overlaps'. In these zones, deformation can occur either by slip on the phyllosilicates at the zone margins accommodated by shearing of the clast overlaps, or by slip on the curved foliation accompanied by dilatation at extensional clast–matrix interface sites. Sliding on the foliation is assumed to be a purely frictional process, which implies that slip on the curved foliation will not occur unless a critical value of the macroscopic shear stress, τ_{dil}, is attained. When slip is activated, it will cause dilatation and porosity development. The authors assumed that developing porosity concentrates at the extensional quartz–illite interfaces (Supplementary Fig. 3), resulting in a decrease in the clast overlap distance, and hence in the mean inclination of the curved foliation. This in turn causes a decrease in the rate of dilation per unit horizontal displacement on the inclined foliation—that is, a decrease in the dilatation angle ψ_{dil}, with increasing porosity. The authors assumed that the appearance of porosity, via clast/matrix debonding, initiates compaction by thermally activated deformation of the clasts, which accelerates as porosity increases. At steady state, dilation due to slip on the curved foliation and compaction by the thermally activated mechanism must balance. This competition between dilatation and compaction is of key importance since it will lead to higher steady-state porosities, a flatter foliation and lower frictional strength as sliding velocity increases, and hence to velocity-weakening slip. This as opposed to non-dilatant deformation, where the serial nature of deformation implies that the velocity dependence of friction is governed by thermally activated deformation of the quartz clasts, which is by definition velocity strengthening. Dilatation, when active, is assumed to continue until a limiting or critical state porosity is reached.

The model does not strictly apply to muscovite. However, in the absence of a microphysical model for the steady-state frictional behaviour of muscovite–quartz fault gouge, and since muscovite–quartz gouge shows broadly similar behaviour to illite–quartz gouge[28], we have applied this model also at temperatures >300 °C, where muscovite is expected to be the dominant phyllosilicate.

Model calculations. The reader is referred to ref. 25 for the derivation of the equations governing the steady-state frictional behaviour of the model microstructure shown in Supplementary Fig. 3 and described below.

The derivations for the unit cell shown in Supplementary Fig. 3b, which has a horizontal dimension equal to horizontal clast spacing:

$$L = \frac{k_f \pi D^2}{(D - x_0) f_{qtz}} \tag{6}$$

where k_f is a factor accounting for clast shape, D is grain size (clast diameter), f_{qtz} is the volume fraction of quartz clasts, and x_0 is the vertical overlap of the clasts at zero porosity, defined as:

$$x_0 = D\left(1 - \sqrt{\frac{k_f\pi}{2f_{qtz}}}\right) \tag{7}$$

As porosity, ϕ, increases due to dilatational slip on the curved foliation, this overlap decreases from x_0 to an instantaneous value x according to the relation $x=(x_0-\phi D)/(1-\phi)$. The decrease in overlap in turn leads to a decrease in the width, d, of overlapping clast segments (Supplementary Fig. 3b), given $d=2\sqrt{(Dx-x^2)}$.

During non-dilatant deformation at low slip velocities and/or high temperatures, thermally activated shear deformation of the quartz clasts will be easy. The total resistance to slip on the horizontal foliation will then be lower than the shear stress to activate slip and dilatation on the anastomosing foliation. Under these conditions, the authors assumed that non-dilatant deformation takes place by the two parallel processes of slip on the horizontal foliation with serial shear of the clast bodies in the B zones of the microstructure plus slip on the horizontal phyllosilicates with serial shear of clast overlaps at the margin of the O zones. Equilibrium between the shear stresses supported by the B and O zones (τ_B and τ_O, respectively) requires $\tau_m=\tau_B=\tau_O$, where τ_m is the macroscopic shear stress. The shear stresses in the B and O zones were derived:

$$\tau_B=\tau_{ph}\left(1-\frac{A_{qtz-B}}{LD}\right)+\tau_{qtz-B}\frac{A_{qtz-B}}{LD} \quad (8)$$

$$\tau_O=\tau_{ph}\left(1-\frac{A_{qtz-O}}{LD}\right)+\tau_{qtz-O}\frac{A_{qtz-O}}{LD} \quad (9)$$

where τ_{ph} is the shear stress needed to drive frictional slip on the horizontal phyllosilicate foliation and τ_{qtz-B} and τ_{qtz-O} are those needed to drive thermally activated clast body and overlap deformation, respectively. A_{qtz-B} represents the average horizontal area occupied by a single clast body within zone B of the unit cell, and is given $A_{qtz-B}=[(1/4\pi D^2-2A'_{seg})D]/(D-2x)$, where $A'_{seg}=[16x^2(D-x)+3x^3]/[12\sqrt{(Dx-x^2)}]$ (ref. 56) is the area of an individual clast segment located in the overlap zone of the cell in the plane of Supplementary Fig. 3 and $A_{qtz-O}=dD=2D\sqrt{(Dx-x^2)}$ is the area over which the overlap is displaced by slip at its base. Note that $\tau_{ph}=\mu_{ph}\sigma'_n$, where μ_{ph} is defined by equation (4).

The two parallel shear processes operating in the O and B zones mean that the total, measured shear strain rate during non-dilatant deformation is $\dot\gamma_m=\dot\gamma_B+\dot\gamma_O$, where $\dot\gamma_B$ and $\dot\gamma_O$ denote the shear strain rate contributed to the unit cell by each zone, respectively (that is, $\dot\gamma_B$ and $\dot\gamma_O$ are determined by taking into account the thickness of the B or O zone relative to the unit cell thickness). Note that the serial coupling of rate-independent slip on the phyllosilicates with thermally activated deformation of clasts implies that $\dot\gamma_B=\dot\gamma_{qtz-B}$ and $\dot\gamma_O=\dot\gamma_{qtz-O}$, where $\dot\gamma_{qtz-B}$ and $\dot\gamma_{qtz-O}$ are the shear strain rate contributions to the unit cell due to thermally activated deformation of the clast bodies and clast overlaps, respectively. Thermally activated deformation was assumed to occur via pressure solution, yielding:

$$\dot\gamma_{qtz-B}=\frac{AI\tau_{qtz-B}\Omega}{RT}\frac{D-2x}{D(D-x)} \quad (10)$$

$$\dot\gamma_{qtz-O}=\frac{2I\tau_{qtz-O}\Omega}{RT}\frac{1}{\sqrt{Dx-x^2}} \quad (11)$$

where A is a shape factor, I is the product of the dissolution rate coefficient k_+ and molar volume Ω of quartz, and R is the gas constant.

Following the authors, we obtained τ_m as a function of $\dot\gamma_m$, by first imposing $\dot\gamma_m$, defined as $\dot\gamma_m=V/w$, where w is the shear zone width. We next solved $\dot\gamma_m=\dot\gamma_B+\dot\gamma_O$ together with $\tau_m=\tau_B=\tau_O$ to obtain $\dot\gamma_B$ or $\dot\gamma_{qtz-B}$. We subsequently used $\dot\gamma_{qtz-B}$ to determine τ_{qtz-B} via equation (10). The value of τ_{qtz-B} obtained then yielded $\tau_B=\tau_m$ through equation (8). Note that in the current calculations we prevented $\dot\gamma_O$ from taking a negative value in the non-dilatant regime[57].

At high slip rates or low temperatures, thermally activated shear deformation of the quartz clasts is difficult, leading to an increase in the total resistance to shear on the horizontal foliation. In the model microstructure this would ultimately activate slip on the curved phyllosilicates in the overlap (O) zones of the microstructure. The measured shear strength in that case is equal to that required to activate slip on the anastomosing foliation, τ_{dil}, derived to be:

$$\tau_{dil}=\left\{\frac{\mu_{ph}(1+\tan^2\Psi_{fr})}{1-\mu_{ph}^2\tan^2\Psi_{fr}}\right\}\sigma'_n \quad (12)$$

where $\tan\Psi_{fr}$ is a straight line approximation of the curved foliation, that is,

$$\tan\Psi_{fr}=\frac{2(D-x_0)f_{qtz}}{k_f\pi D^2}x \quad (13)$$

Stress equilibrium between B and O zones means that in the dilatant case $\tau_m=\tau_{dil}=\tau_B=\tau_O$. The total shear strain rate $\dot\gamma_m$, in turn, is given $\dot\gamma_m=\dot\gamma_B+\dot\gamma_O+\dot\gamma_{dil}$, or equivalently $\dot\gamma_m=\dot\gamma_{qtz-B}+\dot\gamma_{qtz-O}+\dot\gamma_{dil}$, where $\dot\gamma_{dil}$ is the shear strain rate contribution to the unit cell by dilatant slip on the curved phyllosilicates. This mechanism produces an associated dilational strain rate, $\dot\varepsilon_{dil}$, which was defined following the classical soil mechanics approach to granular flow, that is:

$$\dot\varepsilon_{dil}=\left(\frac{d\varepsilon_{dil}}{d\gamma_{dil}}\right)\frac{d\gamma_{dil}}{dt}=(\tan\Psi_{dil})\dot\gamma_{dil} \quad (14)$$

The dilatation angle Ψ_{dil} was defined as the steepest portion of the curved, that is, sinusoidal, foliation:

$$\tan\Psi_{dil}=\sqrt{\frac{\pi f_{qtz}}{2k_f}}-\frac{\pi}{2(1-\phi)} \quad (15)$$

This angle (Ψ_{dil}) decreases with increasing porosity, reaching zero at a limiting or 'critical state' porosity, defined by $\phi_c=x_0/D$ when $x=0$.

The porosity generated by dilatant slip will induce compaction by thermally activated deformation of the quartz clasts at a rate $\dot\varepsilon_{comp}$. Taking compaction as positive, the total, measured compaction strain rate is therefore given $\dot\varepsilon_m=\dot\varepsilon_{comp}-\dot\varepsilon_{dil}$. At steady state, dilatation and compaction must balance, resulting in a steady-state porosity corresponding to the condition that $\dot\varepsilon_m=0$ or $\dot\varepsilon_{comp}=\dot\varepsilon_{dil}$. Following the authors, $\dot\varepsilon_{comp}$ is given by:

$$\dot\varepsilon_{comp}=\frac{2I\sigma'_n\Omega}{RT}\frac{A_{pore}}{(D-x)DL} \quad (16)$$

Compaction occurs by pressure solution transfer from compressively stressed illite–quartz interfaces to debonded (dilated) interfaces (pore walls) with surface area A_{pore}, written $A_{pore}=(A_{pore-c}/2)(\phi/\phi_c)^n$, where ϕ_c and A_{pore-c} are the porosity and pore area per clast at the critical state. The authors derived that $A_{pore-c}=(\pi D^2)/2$.

To calculate τ_m as a function of $\dot\gamma_m$ in the dilatant regime, we followed the procedure in ref. 25 and incremented the porosity from 0 to ϕ_c, and then calculated the corresponding values of $\tan\Psi_{dil}$ and $\tan\Psi_{fr}$ using equations (15) and (13). Using $\tan\Psi_{fr}$, equation (12) gives τ_{dil}. The corresponding shear strain rate $\dot\gamma_m$ is calculated via $\dot\gamma_m=\dot\gamma_{qtz-B}+\dot\gamma_{qtz-O}+\dot\gamma_{dil}$ and using the flow laws in equations (10) and (11). Here, $\dot\gamma_{dil}$ is obtained via equation (14) and using the steady-state condition $\dot\varepsilon_{comp}=\dot\varepsilon_{dil}$, where $\dot\varepsilon_{comp}$ is calculated using equation (16).

In our calculations, we assumed cylindrical quartz clasts ($k_f=0.25$) of either 10 or 100 μm in diameter, taking up a volume fraction of 0.45. Following the authors, we assume that pressure solution is controlled by the interfacial reactions of dissolution and precipitation, and can be described using the empirical equation for the dissolution rate coefficient provided in ref. 37:

$$k_+=276\exp\left(\frac{-90{,}100}{RT}\right) \quad (17)$$

with T in Kelvin. We used a shape factor A of π in our calculation of the clast body shear strain rate, while a factor of 2 was used in the original model. We also follow the assumption that the porosity can be characterized by an exponent n of 0.3 (ref. 25).

To determine our shear strength versus depth profiles predicted by the microphysical model, we selected σ'_n, T and the corresponding μ_{ph} at each depth. Using this input, we obtained τ_m as a function of $\dot\gamma_m$ (incorporating both non-dilatant and dilatant deformation) following the above procedure. We next used the assumed subduction velocity of 40 mm yr^{-1} and shear zone thickness (1 to 100 m in the current calculations) to select the relevant $\dot\gamma_m$, and determined τ_m at that shear strain rate.

The result of our calculations, shown in Fig. 2, yield dilatant deformation at shallow depths and low temperatures for the shear strain rates explored in this study. With increasing depth and temperature, shear deformation of the quartz clasts by pressure solution becomes easier, resulting in a transition to non-dilatant deformation. To illustrate this effect, we show the calculated values of τ_{ph} and τ_{qtz-B} (for non-dilatant shear), and the inferred shear stress as a function of depth, for the scenario where D is 100 μm, w is 100 m, and λ is 0.95, in Supplementary Fig. 4. For any given set of conditions, the transition to non-dilatant deformation depends on strain rate, and we plot the strain rate at which the transition occurs, as a function of depth, in Fig. 3c.

Code availability. Code and additional data are available from the authors on request.

Data availability. The data that support the findings of this study are available from the corresponding author on request.

References

51. Lamb, S. Shear stresses on megathrusts: implications for mountain building behind subduction zones. *J. Geophys. Res.* **111,** B07401 (2006).
52. Wada, I., Wang, K., He, J. & Hyndman, R. D. Weakening of the subduction interface and its effects on surface heat flow, slab dehydration, and mantle wedge serpentinization. *J. Geophys. Res.* **113,** B04402 (2008).
53. McCaffrey, R., Wallace, L. M. & Beavan, J. Slow slip and frictional transition at low temperature at the Hikurangi subduction zone. *Nat. Geosci.* **1,** 316–320 (2008).

54. Byerlee, J. D. Friction of rocks. *Pure Appl. Geophys.* **116,** 615–626 (1978).
55. Tembe, S., Lockner, D. A. & Wong, T.-F. Effect of clay content and mineralogy on frictional sliding behaviour of simulated gouges: binary and ternary mixtures of quartz, illite and montmorillonite. *J. Geophys. Res.* **115,** B03416 (2010).
56. Harris, J. W. & Stocker, H. *Handbook of Mathematics and Computational Science* (Springer, 1998).
57. Noda, H. Implementation into earthquake sequence simulations of a rate- and state-dependent friction law incorporating pressure solution creep. *Geophys. J. Int.* **205,** 1108–1125 (2016).